Ultrafast Rydberg-state dissociation in oxygen: Identifying the role of multielectron excitations

Alexander Plunkett, Nathan Harkema, Robert R. Lucchese, C. William McCurdy, and Arvinder Sandhu

Phys. Rev. A **99**, 063403 — Published 6 June 2019

DOI: 10.1103/PhysRevA.99.063403

Ultrafast Rydberg State Dissociation in Oxygen: Identifying the Role of Multielectron Excitations

Alexander Plunkett,[1] Nathan Harkema,[1] Robert R. Lucchese,[2] C. William McCurdy,[2,3] and Arvinder Sandhu[1,*]

[1] *Department of Physics, University of Arizona, Tucson, AZ, 85721 USA*

[2] *Chemical Sciences Division, Lawrence Berkeley National Laboratory, Berkeley CA 94720, USA*

[3] *Department of Chemistry, University of California, Davis, CA 95616, USA*

Abstract

We investigated the fragmentation dynamics of highly excited states of molecular oxygen using femtosecond transient photoelectron spectroscopy. An extreme ultraviolet (XUV) pulse populates the autoionizing Rydberg series converging to $O_2^+ c\ ^4\Sigma_u^-$, and a femtosecond near-infrared (IR) pulse was used to photoionize these states as they dissociate. Monitoring the differential photoelectron spectra as a function of time delay allowed us to obtain the relaxation lifetimes of these Rydberg states. We observed a photoelectron signal corresponding to the formation of a 4p excited atomic oxygen fragment, which is not an expected dissociation product of the $(O_2^+ c\ ^4\Sigma_u^-)nl\sigma_g$ Rydberg series. Analysis of the time-dependent photoelectron spectra and photoionization calculations indicate that this fragment results from a previously unexplored $(O_2^+\ ^4\Pi_g)4p$ repulsive state and that, contrary to expectations, this multielectron excitation pathway presents a substantial cross section. Our study demonstrates that two-color time-resolved differential photoelectron spectroscopy is an excellent tool to study the fragmentation dynamics of such multi-electron excited states, which are not easily probed by other means.

* asandhu@email.arizona.edu

I. INTRODUCTION

Highly excited molecular states, formed through the interaction of XUV radiation with small molecules [1, 2], play an important role in many physical and chemical phenomena. Examples include solar radiation induced photochemistry of planetary atmospheres [3], the radiation damage of DNA [4], and dissociative recombination of electrons with molecular ions in the interstellar medium [5]. It is well known that single excitations of valence or inner valence electrons to Rydberg molecular orbitals form neutral states that lie above the ionization threshold [6]. Energetically, these states lie above several excited states of the molecular ion into which they can decay through autoionization [7]. These states also exhibit strong configuration mixing and coupled electronic and nuclear motions, which can result in ultrafast dissociation into excited neutral fragments [8]. However, little is known about the dynamics of neutral states formed through multielectron excitations, which typically present a featureless photoabsorption spectra due to their highly repulsive nature and extremely fast fragmentation dynamics.

High-harmonic generation (HHG) can produce photons in the energy range from 10's to 100's eV with femtosecond (10^{-15} s) and attosecond (10^{-18} s) pulse durations [9] to coherently prepare, probe, and control ultrafast dynamics of the highly excited molecules. Combined with time-delayed near infrared (NIR) or visible laser pulses, pump-probe spectroscopy schemes can be used to investigate electron and nuclear dynamics in atoms and molecules [10–15]. In this paper, we employ transient photoelectron spectroscopy to gain new insights into the fragmentation dynamics of single and multielectron excited neutral states in oxygen.

Previous ultrafast pump-probe studies have employed XUV photons in the energy range of 23-25 eV to explore the dynamics of singly excited neutral states of O_2 using pump-probe velocity map imaging (VMI) [16, 17] and attosecond transient absorption [18]. The excited ionic state $c\ ^4\Sigma_u^-$ of the oxygen molecule is formed with the ionization of a $2\sigma_u$ electron. Excitation, rather than ionization, of this electron results in the neutral autoionizing Rydberg series converging to the $c\ ^4\Sigma_u^-$state: $O_2(O_2^+ c\ ^4\Sigma_u^-)nl\sigma_g\ ^3\Sigma_u^-$, abbreviated hereafter as simply $nl\sigma_g$.

Codling and Madden [19] identified two such series in the static XUV photoabsorption spectrum, which have been categorized as $ns\sigma_g$ and $nd\sigma_g$. A weaker $nd\pi_g$ series has

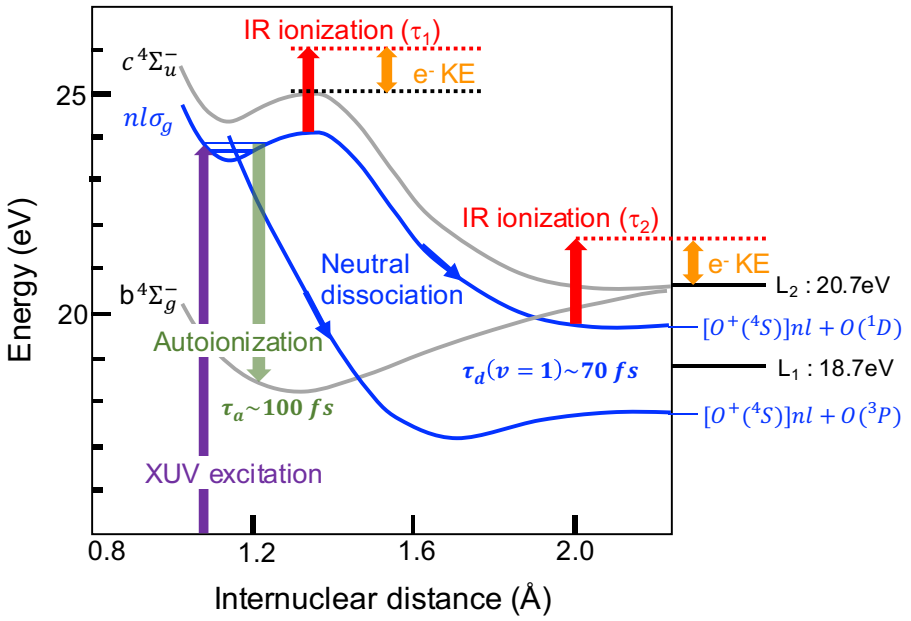

FIG. 1. Sketch showing excited ionic states $c\ ^4\Sigma_u^-$ and $b\ ^4\Sigma_g^-$ of the O_2 molecule. The neutral $nl\sigma_g$ Rydberg state associated with the $c\ ^4\Sigma_u^-$ ionic state contains two vibrational levels, and exhibits autoionization to $b\ ^4\Sigma_g^-$ state and simultaneous dissociation to the neutral Rydberg fragments, with timescales τ_a and τ_d, respectively. A single IR photon is used to ionize the Rydberg state in the molecular or atomic regime as a function of the time delay (τ), and the electron kinetic energy (KE) is recorded. The dissociation pathway forming $(\mathrm{O}^+(^4S))nl\ ^3(S,D)$ + $\mathrm{O}(^1D)$ atoms corresponds to ionic L2 limit, while $(\mathrm{O}^+(^4S))nl\ ^3(S,D)$ + $\mathrm{O}(^3P)$ represents the L1 ionic limit.

been reported in [18, 20]. The properties of the $ns\sigma_g$ and $nd\sigma_g$ series have been studied extensively using synchrotron radiation in photoionization efficiency experiments [21, 22], threshold photoelectron-photoion coincidence [23–26], photoionization mass-spectrometry [27, 28], photoelectron spectroscopy [29, 30], photon-induced fluorescence spectroscopy [31–35], threshold electron spectroscopy [36], vector correlation experiments [37], neutral particle detection [38], photoelectron-photoion coincidence imaging [39] and numerous theoretical efforts [20, 40, 41]. Furthermore, electron impact studies [42, 43] have been used to access optically forbidden series, $2\sigma_u^{-1}(c\ ^4\Sigma_u^-)np\sigma_u\ ^3\Sigma_g^-$, which are not observed in XUV photoexcitation/photoionization studies.

In the ion-core approximation [44], the potential energy curves for Rydberg states are generally very well approximated as curves parallel to the ionic $c\ ^4\Sigma_u^-$ state (Fig. 1). There-

fore, rotational and vibrational spectra as well as the dissociation dynamics of the Rydberg states closely mimic that of the ionic $c\ ^4\Sigma_u^-$ state. Two vibrational levels bound in the $nl\sigma_g$ states have been observed, namely $v = 0$ and $v = 1$. As shown in Fig. 1, the $v = 1$ level is bound by a small potential barrier and and it dissociates quickly via quantum tunneling with a lifetime of $\sim$ 70fs [44, 45] to the adiabatic (L2) limit, $O^+(^4S)nl$+$O(^1D)$. The $v = 0$ state, however, cannot efficiently tunnel through the potential barrier and has a much longer dissociation lifetime, approximately 1100 fs [16]. Dissociation for this vibrational state leads to both the L2 limit, via tunneling and possible curve crossings, and to the L1 limit, $O^+(^4S)nl$+$O(^3P)$, via spin-orbit coupling [23]. The $nl\sigma_g$ Rydberg states also exhibit fast autoionization which competes with neutral dissociation. The autoionization time scale for some of the Rydberg levels have been directly measured [16] to be in the 10's to 100's of femtoseconds, with longer lifetimes corresponding to larger effective quantum number of Rydberg states. Comparable autoionization and dissociation rates imply that for the $v = 1$ Rydberg states both autoionization and neutral dissociation are important decay mechanisms, whereas the $v = 0$ Rydberg states mostly autoionize to low lying ionic states with only a small fraction undergoing dissociation.

Neutral dissociation separates the molecule into two atoms, one of which is in an atomic Rydberg state. The exact products of the Rydberg dissociation are relatively simple to enumerate, and can be explained as conservation of effective principal quantum number. As put forth in Liebel *et al.* [34], the $ns\sigma_g$ states dissociate into atomic $(^4S)(n-1)d\ ^3D_J$ and $ns\ ^3S_1$ states while the $nd\sigma_g$ states dissociate into atomic $(^4S)(n+1)s\ ^3S_1$ and $(^4S)nd\ ^3D_J$ states.

II. EXPERIMENTAL SETUP

A laser amplifier in our experimental set up produces a 35 fs, 1.8 mJ, IR laser pulse centered at 780 nm which was passed through a beamsplitter as shown in Fig. 2(a). The transmitted beam is focused with a 50 cm mirror into a Xe gas cell where it generates an XUV attosecond pulse train (APT) through HHG. The XUV spectrum predominantly consists of 13th, 15th, and 17th harmonics, and 15th harmonic is centered at 23.8 eV with full width half maximum bandwidth of $\sim$ 0.6 eV. A toroidal mirror at grazing incidence is set up in a 2f-2f geometry to image the XUV source into the velocity map imaging (VMI) chamber. The

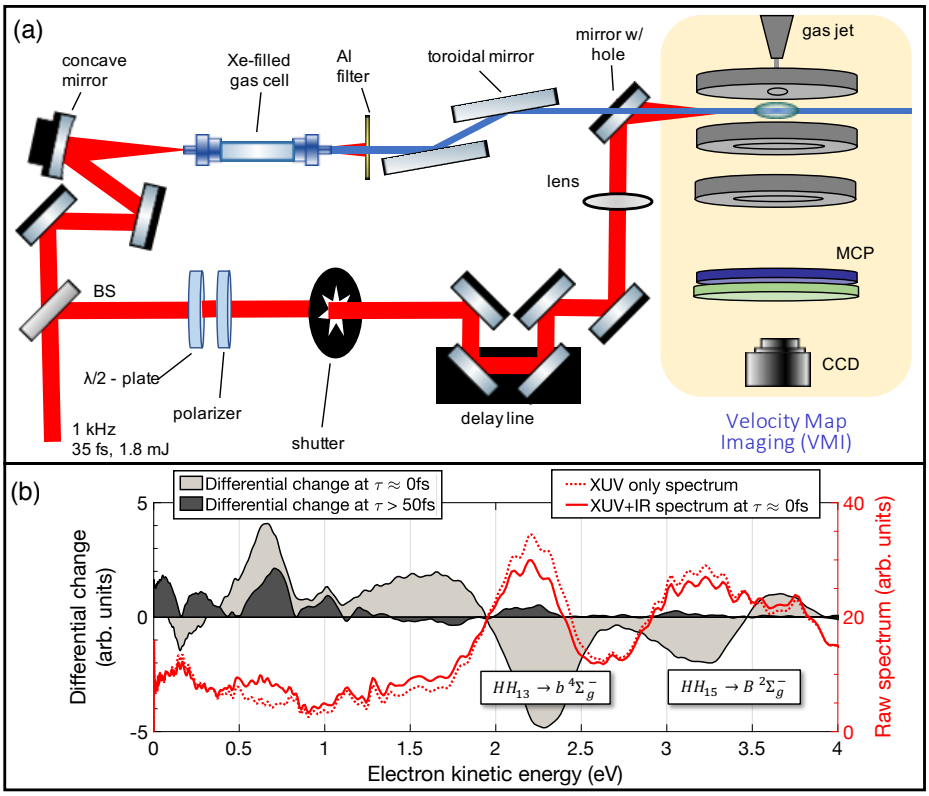

FIG. 2. (a) Schematic of the pump-probe experiment showing XUV beam line consisting of an HHG gas cell, routing optics and a perforated mirror to recombined the time-delayed IR beam. The XUV and IR pulses are focussed into a velocity map imaging setup. (b) Electron spectra produced by angular integration of the reconstructed VMI images for XUV only case (dashed line) and the XUV+IR case at zero time delay (solid line). Subtraction of these datasets yields differential spectra that emphasize the IR induced changes at zero delay, and for delays $\geq$ 50 fs (area plots).

reflected portion of the IR laser pulse is time-delayed and a perforated mirror that allows the XUV beam to go through is used to recombine the IR beam for collinear propagation with the XUV. Both beams are focused into the VMI chamber where they interact with an effusive gas jet. The XUV pulse serves to populate the neutral Rydberg excited states and the time-delayed IR pulse of intensity $\sim 10^{12}$ Wcm^{-2} probes their evolution by one-photon ionization. Electrons produced in this interaction are detected using a dual-MCP plate in chevron configuration and a fast phosphor screen. Electrostatic lenses image the electron momentum in the plane defined by the laser polarization and propagation direction. By performing a pBASEX reconstruction for each time delay we "slice" the 3D momentum

distribution [46]. For each time delay we record two sets of data, one for the two-color, XUV+IR case and one of the XUV only case. Angular integration of the VMI images in each case yields the electron spectra shown in Fig. 2(b) (line plots). Subtracting the two data sets allows us to isolate IR-induced effects in the differential electron spectra as shown in Fig. 2(b) (area plots). Performing this procedure for each IR time delay step produces a transient electron spectrogram with electron kinetic energy on the y-axis and time delay on the x-axis (Fig. 3).

III. RESULTS

The experimentally observed transient electron spectrogram in Fig. 3 highlights the differential changes in the electron spectrum by the action of a time-delayed probe pulse. At negative time delays the IR field arrives before the XUV APT. At these time delays we measure no IR-induced changes in the photoelectron spectrum, indicated by the absence of any features at negative time delays. When the two pulses are overlapped, the XUV light populates the $nl\sigma_g$ states and the IR pulse is able to ionize them. Energetically, the $nl\sigma_g$ Rydberg states are ordered as pairs with $(n-1)d$ and ns configuration, and one-photon IR ionization of these states produces electron with kinetic energies indicated by horizontal black lines on the left of Fig. 3, labeled pairwise as $4d/5s\sigma_g$, $5d/6s\sigma_g$, and so on. After time zero, IR pulse can ionize the Rydberg states that have not autoionized, whether or not they have dissociated. In other words, both the excited molecules and the excited atoms formed by dissociation are being probed with the IR field. Thus, the decay of the IR ionization signal in Fig. 3 (and in Fig. 4) is due to the autoionization of Rydberg states and is sensitive to the predissociation lifetime only in that separating the nuclei "turns off" the autoionization. The expected electron kinetic energies from atomic Rydberg ionization are indicated by the horizontal black lines on the right side of Fig. 3 and represent the $ns\ ^3S$ and $nd\ ^3D$ atomic state pairs. The data indicate that dissociation occurs rapidly and flat asymptotic behavior in electron energy spectrum is observed on timescales less than 150 fs.

Negative features in the transient electron spectrogram are produced when IR pulse scatters the direct XUV photoelectrons, thereby depleting the electron yield at that kinetic energy. For example, the dip near ~ 0.2 eV at zero time delay results when continuum electrons emitted in the direct XUV ionization from ground state to the $B\ ^2\Sigma_g^-$ ionic state

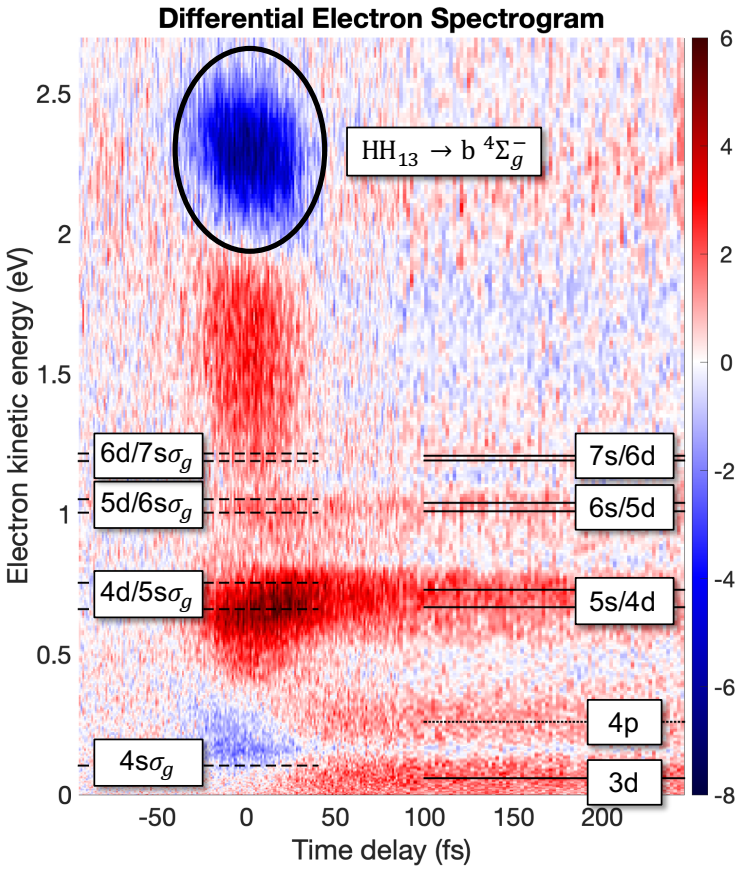

FIG. 3. (Color online) Transient electron spectrogram which represents the difference between XUV+IR and XUV only data. Positive values represent increase in electron yield at that energy due to the IR ionization of Rydberg states, or due to IR sidebands of the direct XUV photoelectrons. Negative features, like the one at 2.3 eV, result when IR pulse scatters the direct XUV photoelectrons. Horizontal black lines on the left and right sides indicate the expected kinetic energies of photoelectrons from molecular and atomic Rydberg states, respectively. Atomic $4p$ fragments are not an expected product of the $nl\sigma_g$ dissociation but we observe IR ionization signal from these fragments at ∼0.3 eV

by the 13th harmonic are dressed by the IR field. This IR dressing leads to XUV photoelectrons gaining one unit of IR photon energy, thus producing a complimentary broad positive sideband centered at ∼1.6 eV. The 13th harmonic also ionizes from ground state to the $b\ ^4\Sigma_g^-$ ionic state, producing 2.3 eV electrons which are similarly dressed by the IR field, leading to depletion at 2.3 eV and positive sideband around 0.7 eV. IR dressing sidebands overlap with the one-photon IR ionization signals from molecular Rydberg states, complicating the data

analysis near zero time delay. However, the IR dressing contamination is not present for time delays greater than 30 fs and electrons from molecular Rydberg states $4s\sigma_g$, $4d/5s\sigma_g$, and $5d/6s\sigma_g$ are clearly observed along with their atomic counterparts $3d$, $5s/4d$, and $6s/5d$, as shown in Fig. 3.

When the IR sidebands are no longer obscuring the Rydberg ionization, we see another electron signal at 0.3 eV, which is an unexpected feature. Energetically, in the dissociation limit, we can identify it with IR ionization from the $4p$ $^{(3,5)}P_J$ atomic states of oxygen. However, based on the commonly accepted viewpoint described in Liebel *et al.* [34], the $4p$ excited fragment does not result from the XUV excited $nl\sigma_g$ states, and there is no prior study identifying other states in the energy range of our harmonics that could lead to these $4p$ excited atomic fragments. To our knowledge, no static synchrotron studies of the autoionizing states of oxygen in this energy regime have not observed fragmentation pathways that could give rise to this feature.

A pump-probe experiment similar to ours [17] observed the $4p$ excited atom formation. In that study, the origin of $4p$ feature was attributed to the dissociation of $nl\sigma_g, v = 0$ Rydberg state based on their observed rise time of $427 \pm 75 fs$. However, our results in Fig. 3 do not exhibit such slow rise time. In fact, we distinctly observe the $4p$ feature reaching a maximum value within 50 fs. For even shorter time delays, the presence of an overlapping IR induced depletion feature masks the Rydberg ionization signals. Thus, in order to quantify the timescale for $4p$ excited atom formation, we need to account for this depletion feature.

In Fig. 4(a) we have plotted the line out of the direct ionization depletion corresponding to IR dressing of electrons produced in 13th harmonic ionization from ground state to the $b\ ^4\Sigma_g^-$ ionic state. This depletion signal is centered at 2.3 eV (Fig. 3), and because there are no Rydberg ionization signals at that energy, we use it to obtain the XUV-IR cross correlation width by fitting it with a Gaussian. The FWHM thus obtained (49 ± 2 fs) helps us to estimate the rise time of $4p$ signal, and account for the contribution of IR dressing sidebands to various Rydberg ionization features.

Fig. 4(b-d) show the time dependence of Rydberg ionization for channels that result in the formation of $6s/5d$, $5s/4d$, and $4p$ excited fragments. Both the $6s/5d$ and $5s/4d$ dissociation channels show a decay related to the lifetime of the metastable $nl\sigma_g$ molecular Rydberg states. The $4p$ dissociation channel, in contrast, reaches a maximum value within the XUV-IR cross correlation width and does not decay. This indicates that the $4p$ atomic

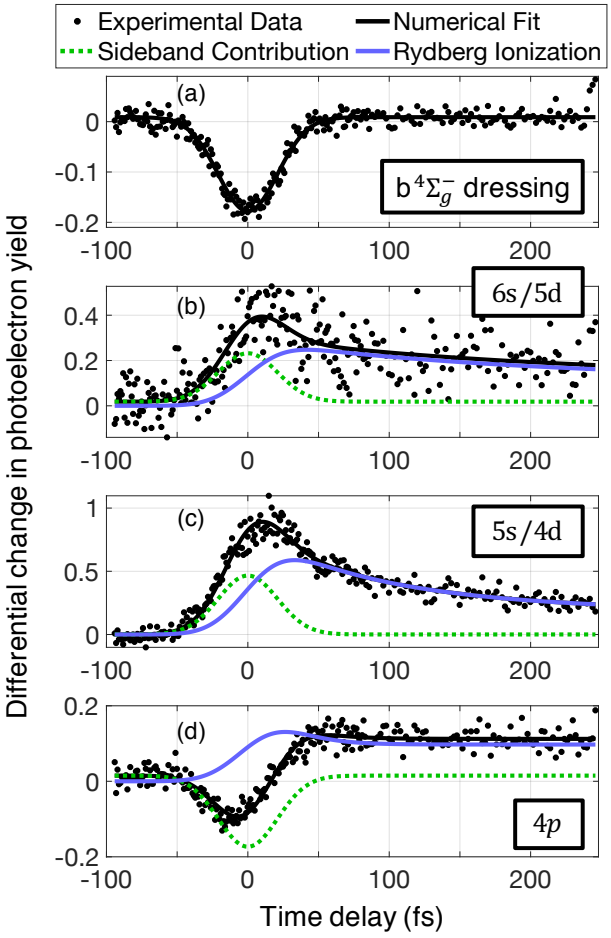

FIG. 4. (Color online) The delay dependent line outs for several important features in Fig. 3 with averaging over ∼100 meV energy window. (a) IR dressing induced depletion of direct photoelectrons corresponding to $b\ ^4\Sigma_g^-$ continuum, (b) IR ionization of $6s/5d\sigma_g$ molecular Rydberg state pair, (c) $5s/4d$ pair, and (d) the feature corresponding to formation of $4p$ excited atomic fragment. In all plots, the solid blue (grey) curve represents the combined electron yield contribution from molecular Rydberg states and excited atomic fragments, the dashed green (light grey) curve the overlapping IR dressing contribution, and the solid black curve the sum of all contributions.

fragment is not produced by dissociation of the relatively long-lived $nl\sigma_g$ Rydberg series and must arise from a different pathway.

To develop this interpretation further, we used a first-order rate equation model to fit the photoionization yield of the $nl\sigma_g$ channels based on the autoionization and predissociation rates of the molecular states. In the model (fully described in the Appendix A), the total ionization yield is fitted by adding contributions from (1) molecular Rydberg photoionization,

(2) excited neutral fragment photoionization, and (3) IR dressing sideband. The combined contribution from the molecular Rydberg and excited atomic fragments is plotted in Fig. 4(b,c) as solid blue (grey) lines. The dressing sideband contribution to the total electron yield is plotted as a green (light grey) dashed line. The sideband contribution is a Gaussian whose width is determined by the XUV-IR cross correlation obtained from the fit in Fig. 4(a). The fits for $5s/4d$ and $6s/5d$ fragments allowed us to estimate the autoionization lifetimes of corresponding molecular states as, 115±16 fs and 285±169 fs, respectively, which are comparable to our previous measurements [16].

In Fig. 4(d), we attempted the same fitting procedure for 0.3 eV $4p$ atomic fragment ionization signal. At this energy, rather than a positive dressing sideband, we have an overlapping negative depletion feature at zero time delay associated with the scattering of direct electrons produced in ionization to the $B\ ^2\Sigma_g^-$ ionic state. Thus, the fit for the $4p$ photoelectron signal included a negative Gaussian, again with width specified by the XUV-IR cross correlation obtained in Fig. 4(a). If we assume that the 4p signal arises from a metastable molecular state with significant autoionization and predissociation rates, similar to the $nl\sigma_g$ series, we obtain a dissociation timescale smaller than the XUV-IR cross correlation width, i.e. faster than the time resolution of the experiment. This result strongly indicates that $4p$ fragments are produced in a rapid dissociation process which completes before significant autoionization can occur.

The above findings on the formation of $4p$ excited fragment are in contrast to the evolution of the $nl\sigma_g$ molecular Rydberg states (Fig. 4(b-d)), as well as Ref. [17]. In Ref. [17], the authors proposed the slow decay of the $v = 0$ level of the $4s\sigma_g$ molecular Rydberg state as a potential mechanism for forming $4p$ atomic fragments on the timescale of ($\sim$ 427 fs). Our results show a strong evidence of fast rise time ($\leq$ 45 fs) of $4p$ signal, indicating a prompt dissociation mechanism. To further solidify our results, we investigated the IR ionization yield for the $4p$ excited atomic fragment in time delay scans going as far as 1000 fs and compared it with the other signals unambiguously arising from $nl\sigma_g$ series. A comparison of electron spectra at 170 and 900 fs is shown in Fig. 5. Photoelectron peaks at 0.7, 1.0 and 1.2 eV, corresponding to the $5s/4d$, $6s/5d$, and $7s/6d$ limits, exhibit significant drops in intensity due to autoionization accompanying the slow dissociation of molecular states, whereas the $4p$ signal intensity at 0.3 eV does not decrease with time. This again confirms a very fast dissociation process in which there are no molecules left to autoionize and decrease

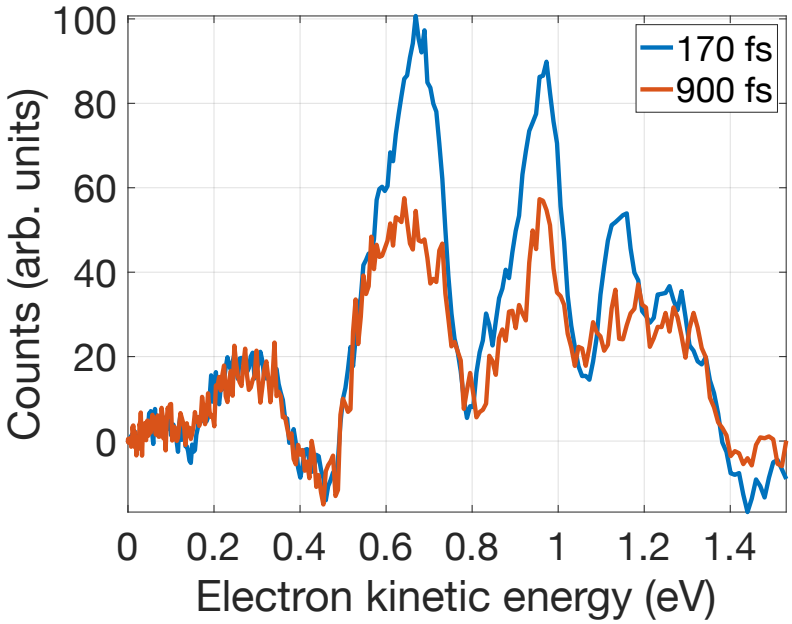

FIG. 5. A comparison of electron spectra taken at 170 fs and 900 fs time delay, with a 50 fs integration window. At 900 fs the signals from the 5s, 6s, and 7sσ_g molecular Rydberg states between 0.5 and 1.25 eV are depleted through autoionization but the 4p signal at 0.3 eV maintains intensity.

the Rydberg photoionization at longer time delays. Thus our experimental work strongly points to the fact that the long-lived metastable states in the $c\ ^4\Sigma_u^- nl\sigma_g$ series are not the origin of the 4p excited atomic fragment. This fragment must result from a different dissociation pathway unreported in the literature.

IV. DISCUSSION

To identify the mechanism of production of the $O^+(^4S)4p$ fragment that we observe, we performed calculations on the O_2^+ ionic states to approximately locate the molecular Rydberg states associated with them, assuming that the Rydberg state potential energy curves are approximately parallel to those of the corresponding ion parent states. Those calculations employed an aug-cc-pVTZ basis and a complete-active-space self-consistent field (CASSCF) description of the ground state with a complete active space (CAS) distributing the electrons among the valence orbitals of O_2 while keeping the $1\sigma_g$ and $1\sigma_u$ core orbitals doubly

occupied. Then the ion states were computed using the internally-contracted multi-reference configuration interaction (ic-MRCI) capability of MOLPRO [47, 48] suite of quantum chemistry programs.

A selection of those ionic states is plotted in Fig. 6. The lowest ion curve shown is a $^4\Pi_g$ state that correlates with O and O^+ dissociation products in their ground states. The attachment of a $4p$ Rydberg electron to this steeply repulsive state gives rise to $^3\Sigma_u^-$ and $^3\Pi_u$ states (and others), which would be approximately parallel to the ionic curve and lie about 1.26 eV below it (the binding energy of the $4p$ electron in the $O^+(^4S)4p$ atomic state). The $^3\Sigma_u$ and $^3\Pi_u$ molecular Rydberg states can explain the fast formation of $4p$ fragments, and they can be reached in optically allowed transitions from the O_2 $^3\Sigma_g^-$ ground state [49]. However, intensities for these transitions might be expected to be relatively weak since they require multielectron excitation. The XUV transition from the $^3\Sigma_g^-$ ground state, with electronic configuration $\ldots\pi_u^4\pi_g^2$, to the final state $O_2^+(^4\Pi_g)4p$ involves promotion of two π_u electrons: one to the π_g forming $^4\Pi_g$ ion core described by the electronic configuration $\ldots\pi_u^2\pi_g^3$, and another to the outer Rydberg orbital, e.g. $4p\pi_u$. In other words, the only non-zero contributions to the transition matrix element come from the small correlating terms in the $^3\Sigma_g^-$ wave function, e.g. $\ldots\pi_u^2\pi_g^4$.

To estimate the population of the $O_2^+(^4\Pi_g)4p$ Rydberg state relative to the populations of the $O_2^+(c\ ^4\Sigma_u^-)5s$ and $4d$ Rydberg states, we have performed photoionization calculations that are very similar to those reported in Ref. [18]. The photoionization calculations were performed using the Schwinger variational method [50, 51] in which the final-state fixed-energy photoelectron wave functions are represented on a single-center expanded grid. The full N-electron ionized state was then written as a close-coupling expansion containing a sum of the products of $(N-1)$-electron ion state wave functions times one-electron photoelectron wave functions. In contrast to the earlier study [18], here we have not adjusted the ionization potentials of the various ion states, but instead we have used the configuration interaction (CI) energies for the ion states found in the Schwinger photoionization calculation. Note that the ion state energies in the photoionization calculations are thus slightly different from the ion states energies computed using the ic-MRCI method that are shown in Fig. 6 which contain significantly more correlation. In the photoionization calculations, the ionization potentials at $R = 2.30$ Bohr were 24.08 eV for the $^4\Pi_g$ state and 25.25 eV for the $c\ ^4\Sigma_u^-$ state. The ion channels used in the close coupling calculation were the $X\ ^2\Pi_g$, $a\ ^4\Pi_u$, $A\ ^2\Pi_u$,

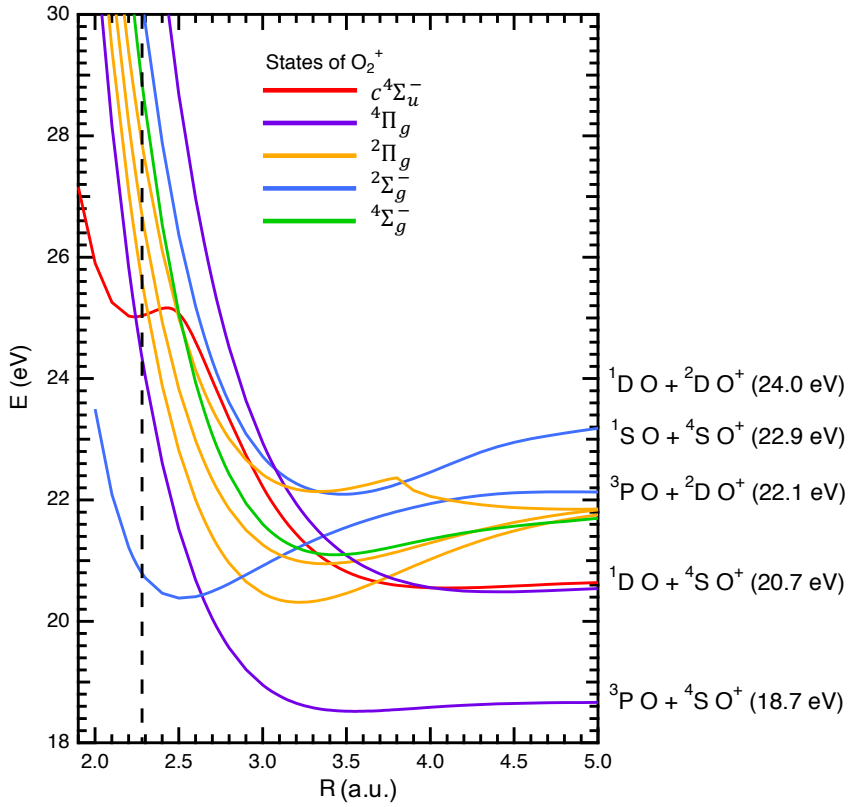

FIG. 6. Potential curves for ionic states of O_2^+ calculated with ic-MRCI whose associated Rydberg states may play a role in O_2 photodissociation, with colors denoting the symmetries of the states. The $3d/4s$ and $4d/5s$ Rydberg states in Fig. 7 are associated with the $c\ ^4\Sigma_u^-$ ion state, while the $4p$ and $5p$ Rydberg states in that figure are associated with the dissociative $^4\Pi_g$ state. The dashed black line represents equilibrium internuclear distance in the ground state.

$b\ ^4\Sigma_g^-$, $B\ ^2\Sigma_g^-$, $^4\Pi_g$, and $c\ ^4\Sigma_u^-$. In Fig. 7 we present the cross sections for ionization in the $^3\Sigma_u^-$ continuum. We can clearly see a sequence of $np\ ^4\Pi_g$ Rydberg autoionization resonances leading up to the threshold at 24.08 eV. Additionally we see two of the $(n)d/(n+1)s$ autoionization features that lead up to the $c\ ^4\Sigma_u^-$ state at 25.25 eV. There are additional unresolved features in the region of the $3d/4s$ resonance which come for overlapping $(^4\Pi_g)np$ resonances.

The populations of the Rydberg states produced by these resonances were then estimated by fitting the cross section features to the Fano line shape given in Eq. (B9) of the Appendix B. In these fits, we assumed that each resonance was independent and that the cross sections could be incoherently summed. In Table I we give the results of these fits for $R = 2.30$ Bohr

and $R = 2.35$ Bohr. We can see that the initial population in the $(^4\Pi_g)4p$ state is comparable to the populations of the $(c\,^4\Sigma_u^-)4d$ and $(c\,^4\Sigma_u^-)5s$ states. This result is due to a combination of the larger values of Γ in the $(^4\Pi_g)4p$ state with smaller σ_{gE} and much smaller f_{gb}. The two geometries presented in Table I correspond to a bond length near the center of the Franck-Condon region, $R = 2.30$ Bohr, and one at the classical outer turning point in the ground vibrational state. We see that there are some quantitative changes over this range of geometries, however the basic conclusion is the same, i.e. there is a substantial initial population in the $(^4\Pi_g)4p$ autoionizing state, which is primarily produced by coupling to the continuum and not due to a direct excitation of the resonant state. Additionally, transitions to autoionizing resonances leading to the $^4\Pi_g$ of O_2^+ state would not correspond to sharp XUV absorption features, because their potential curves are steeply repulsive in the Franck-Condon region leading to diffuse absorption.

TABLE I. Parameters for the Fano profile fits of the $4p\ ^4\Pi_g$, $5s\ c\,^4\Sigma_u^-$ and $4d\ c\,^4\Sigma_u^-$ autoionizing Rydberg states seen in Fig. 7 for $R = 2.30$ Bohr and $R = 2.35$ Bohr. σ_{gE}, q, and Γ were obtained from the fits of the computed cross section for the $^3\Sigma_u^-$ continuum using Eq. (B9). f_{gb} was computed using Eq. (B11). The initial populations were computed relative to the initial population in the $5s\ c\,^4\Sigma_u^-$ Rydberg autoionizing state using Eq. (B8).

State	σ_{gE} (Mbarn)	q	Γ (eV)	f_{gb}	Relative Population
			$R = 2.30$ Bohr		
$4p\ ^4\Pi_g$	3.363	-0.117	0.0408	2.69×10^{-5}	0.913
$4d\ c\,^4\Sigma_u^-$	8.467	0.282	0.0123	1.18×10^{-4}	0.691
$5s\ c\,^4\Sigma_u^-$	7.883	-0.586	0.0153	5.95×10^{-4}	1.000
			$R = 2.35$ Bohr		
$4p\ ^4\Pi_g$	3.392	-0.210	0.0420	8.95×10^{-5}	1.065
$4d\ c\,^4\Sigma_u^-$	8.633	0.462	0.0131	3.46×10^{-4}	0.890
$5s\ c\,^4\Sigma_u^-$	9.200	-0.411	0.0144	3.20×10^{-4}	1.000

Based on the discussion above, we can have another look at the $4p$ data in Fig. 4. Using the autoionization linewidth for $4p$ in the Table I, we can fit the data using the procedure

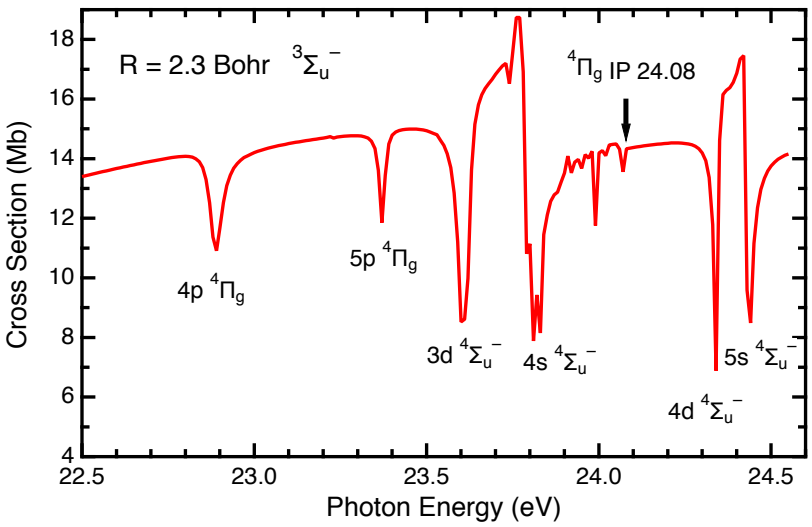

FIG. 7. Photoionization cross section for excitation into the $^3\Sigma_u^-$ continuum from seven channel Schwinger variational calculations including the channels leading to $^4\Pi_g$ and $c\ ^4\Sigma_u^-$ states of O_2^+. There is some unresolved Rydberg autoionization structure within 0.5 eV of the threshold for the production of the $^4\Pi_g$ state which occurs at 24.08 eV. The geometry for this calculation is $R = 2.30$ Bohr which is near the equilibrium of the ground state which occurs at $R_e = 2.28$ Bohr.

described earlier that accounts for the depletion region due to the IR dressing, except here we don't need to account for two vibrational levels. Within the limitations of our modeling, we obtain a dissociation lifetime of 52 ± 15 fs, which verifies that a fast repulsive state is producing $4p$ atomic fragments.

To conclude, we find that XUV excitation by the 15th harmonic generates a significant population of a previously unexplored $(^4\Pi)4p$ Rydberg state in molecular oxygen. This excitation is unresolved in synchrotron experiments due to its strongly repulsive nature and therefore broad and diffuse absorption spectrum. The fragmentation from this channel has also gone undetected in fluorescence studies because its dissociation products cannot directly fluoresce to the ground state. Furthermore, we show that despite the need for multi-electron excitation, the cross section for the $(^4\Pi_g)4p$ state is not negligible, in fact it is comparable to the well-studied $(c\ ^4\Sigma_u^-)nl\sigma_g$ series. We have demonstrated that ultrafast photoelectron spectroscopy is a tool well suited to study such states, and the application of this approach in other systems can help to identify the role of strongly repulsive multi-electron excitations which usually present a flat background absorption spectrum in energy domain studies.

Using few-cycle pulses, one could also probe the transition from the molecular regime to the atomic fragments in a state selective manner. Extension of our approach to multi-pulse, multi-color pump-probe photoelectron spectroscopy can also shed light on the role of dark states in the charge and energy redistribution mechanisms in molecules.

Work at the University of Arizona and the University of California Davis was supported by the U. S. Army Research Laboratory and the U. S. Army Research Office under grant number W911NF-14-1-0383. A.P. was partially supported by National Science Foundation (NSF) award number PHY-1505556. Work performed at Lawrence Berkeley National Laboratory was supported by the US Department of Energy Chemical Sciences, Geosciences, and Biosciences Division Contract DE-AC02-05CH11231.

Appendix A: Modeling $nl\sigma_g$ predissociation and autoionization

To briefly summarize: an XUV pulse populates the two vibrational levels of the molecular $nl\sigma_g$ Rydberg states $v = 0, 1$ at time zero with a 3:1 ratio [37]. Both vibrational states autoionize with rate γ_A, however their predissociation rates differ dramatically, with $\gamma_D(v = 1) = 70$ fs and $\gamma_D(v = 0) = 1100$ fs [16, 45]. Essentially, $v = 0$ states predominantly decay via autoionization, whereas significant dissociation occurs within the autoionization lifetime for the $v = 1$ states. Photoelectrons from molecular and Rydberg states have the same kinetic energy within the resolution of our experiment, so we simultaneously measure both populations. The time dependent population in a particular $(nl\sigma_g, v)$ molecular Rydberg state can be written as

$$P^{Ry}_{mol}(t) = P_0 e^{-\gamma_A t} e^{-\gamma_D t} \tag{A1}$$

where γ_A and γ_D are the autoionization and dissociation rates associated with the particular state. Atomic Rydberg population is determined by the dissociation rate of the associated molecular Rydberg state:

$$\frac{d}{dt} P^{Ry}_{ato}(t) = \gamma_D P^{Ry}_{mol}(t) \tag{A2}$$

Integration over time yields the atomic Rydberg population:

$$P^{Ry}_{ato}(t) = P_0 \left(\frac{\gamma_D}{\gamma_A + \gamma_D} \right) \left(1 - e^{-(\gamma_A + \gamma_D)t} \right) \tag{A3}$$

Finally we can express the total Rydberg population as

$$P^{Ry}_{tot}(t) = P^{Ry}_{mol}(t) + P^{Ry}_{ato}(t) \tag{A4}$$

and the total ionization rate as

$$\frac{dn}{dt}(t,\tau) \propto P_{tot}^{Ry}(t) e^{-\frac{(t-\tau)^2}{2\sigma^2}} \tag{A5}$$

where τ is the time delay of the IR pulse relative to the XUV pulse and σ is the Gaussian width of the XUV-IR cross correlation. By integrating Eq. A5 over time, we get the delay-dependent electron yield $n(\tau)$ for each Rydberg vibrational state as:

$$n(\tau) \propto \frac{\gamma_A}{\gamma_T}\mathrm{EMG}\left(\tau;\gamma_T,\sigma\right) + \frac{\gamma_D}{\gamma_T}\mathrm{EMG}\left(\tau;0,\sigma\right) \tag{A6}$$

where $\gamma_T = \gamma_A + \gamma_D$ is the total decay rate, and EMG stands for exponentially modified Gaussian, defined as:

$$\mathrm{EMG}(\tau;\gamma,\sigma) = \int_0^\infty dt e^{-\gamma t} e^{-(t-\tau)^2/2\sigma^2} = \sigma\sqrt{\frac{\pi}{2}}\exp\left(-\gamma\tau + \frac{\gamma^2\sigma^2}{2}\right)\mathrm{erfc}\left(-\frac{\tau}{\sigma\sqrt{2}} + \frac{\sigma\gamma}{\sqrt{2}}\right) \tag{A7}$$

For each Rydberg state, we sum the contribution from $v = 1$ and $v = 0$ vibrational levels, with $v = 0$ having 3 times greater weight. In addition, we add the contribution of overlapping IR sideband/depletion as a Gaussian of known width determined by the XUV-IR cross correlation. The total electron yield expression thus obtained is used to fit the results in Fig. 4(b-c). In each case, the black curve is the sum of Gaussian sideband contribution (dashed curve) and the Rydberg ionization (Eq. A6) contribution for both vibrational levels (solid blue(grey) curve).

Appendix B: Estimating the population of resonant states from Fano line shapes

In ref. [18] we gave a derivation of a time-dependent version of the Fano analysis of the line shape of autoionizing resonances excited by a pulse of finite duration. The analysis in [18] presumes a discrete state $|b\rangle$ coupled to a continuum $|E\rangle$ by electronic interactions, both of which are dipole coupled to the ground state $|g\rangle$ by the applied XUV field. The case of a Gaussian XUV pulse centered at the resonant frequency $\omega_{\mathrm{XUV}} = \omega_b$, with electric field

$$\mathcal{E}_{\mathrm{XUV}}(t) = F_{\mathrm{XUV}}\ e^{-(t/\tau_{\mathrm{XUV}})^2}/\sqrt{\pi\tau_{\mathrm{XUV}}^2}\exp\left(i\omega_b t\right) + \mathrm{c.c.}, \tag{B1}$$

was treated explicitly, but the final results have the same general form for any pulse shape. The dipole coupling between the ground and discrete states is denoted by D_{gb}, and the

coupling between the ground and continuum states by D_{gE}. The coupling between the discrete state and the continuum is V_{Eb}.

The two results of the previous time-dependent analysis that are relevant here are (1) the population of the discrete state, (given in Eq. C11 of ref [18])

$$C_b(t) = i\, e^{-\Gamma t/2} D^*_{gb}(1 - i/q) F_{\rm XUV} G(t), \tag{B2}$$

written in terms of the conventional Fano parameters,

$$q = \frac{D_{gb}}{\pi D_{gE} V_{Eb}} \quad , \tag{B3}$$

$$\Gamma = 2\pi |V_{Eb}|^2 \quad . \tag{B4}$$

and (2) the photoabsorption cross section that corresponds to the limit of an infinitely short pulse

$$\sigma(\omega) = \sigma_{gE}(\omega) \frac{(\omega - \omega_b + q\,\Gamma/2)^2}{(\omega - \omega_b)^2 + (\Gamma/2)^2}, \tag{B5}$$

where

$$\sigma_{gE}(\omega) = 4\pi^2 \alpha\, \hbar\omega |D_{gE}|^2 \tag{B6}$$

and where α is the fine structure constant.

In the case where the resonance is coupled to a single continuum, the fit of Eq. (B5) to $\sigma(\omega)$ gives four parameters: q, Γ, ω_b and σ_{gE}. Using the definitions of the Fano parameters in Eq.(B4), the population given by Eq.(B2) can be be expressed in the form

$$\begin{aligned} |C_b(t)|^2 &= e^{-\Gamma t} \pi^2 |D_{gE} V_{Eb}|^2 (1 + q^2) |F_{\rm XUV} G(t)|^2 \\ &= e^{-\Gamma t} \frac{\pi \Gamma}{2} |D_{gE}|^2 (1 + q^2) |F_{\rm XUV} G(t)|^2 \,. \end{aligned} \tag{B7}$$

From this result we can make two key observations:

1. The ratios of the populations of any two states, b and b', in this model of the exponentially decaying autoionizing states in the photoionization cross section are

$$\frac{|C_b(t=0)|^2}{|C_{b'}(t=0)|^2} = \frac{\sigma_{gE}(\omega_b)(1 + q_b^2)\Gamma_b}{\sigma_{gE}(\omega_{b'})(1 + q_{b'}^2)\Gamma_{b'}} \frac{\omega_{b'}}{\omega_b} \tag{B8}$$

where σ_{gE}, ω_b, q_b, and Γ_b can be obtained from the fits of each resonance feature.

2. When $q = 0$ the direct dipole coupling, D_{gb}, between the ground and discrete states, $|g\rangle$, and $|b\rangle$, vanishes. The population is then proportional to $|D_{gE}V_{Eb}|^2$ and involves no other coupling, so the discrete state $|b\rangle$ is populated purely by the indirect mechanism of excitation of the continuum together with the coupling between the continuum and discrete states that determines the width.

In other words when $q = 0$ the "dark" discrete state borrows intensity from the "bright" continuum, but when $q^2 >> 1$ the direct dipole coupling D_{gb} is the dominant mechanism for exciting the resonance state.

For a system in which there are many channels, Fano [52] argued in 1961 that the problem can be viewed equivalently in terms of an effective channel that couples to the discrete state via V_{bE} and a noninteracting background. In that case the cross section can be fit in a way that treats the noninteracting background separately, for example as a linear function,

$$\sigma(\omega) = \sigma_{gE}(\omega)\frac{(\omega - \omega_b + q\,\Gamma/2)^2}{(\omega - \omega_b)^2 + (\Gamma/2)^2} + A + B(\omega - \omega_{\rm XUV}) \tag{B9}$$

thus extracting the four relevant parameters appearing in Eq.(B7) from a six parameter fit of the resonance feature in the photoionization cross section. Note that once the line shape has been fit, it is possible to estimate the strength of the direct excitation of the resonant state, $|D_{gb}|^2$, using Eq. (B3) and (B4) to give

$$|D_{gb}|^2 = \frac{\pi}{2}q^2|D_{gE}|^2\Gamma. \tag{B10}$$

The oscillator strength [53] for the direct excitation of the resonant state can then be written as

$$f_{gb} = \frac{1}{2\pi^2\alpha}\left[\frac{\pi}{2}q^2\sigma_{gE}(\omega)\Gamma\right]. \tag{B11}$$

---

[1] U. Becker and D. A. Shirley, *VUV and Soft X-ray Photoionization* (Springer Science & Business Media, 2012).

[2] C.-Y. Ng, *Vacuum ultraviolet photoionization and photodissociation of molecules and clusters* (World Scientific, 1991).

[3] R. P. Wayne, *Chemistry of Atmosphere: An Introduction to the Chemistry of the Atmosphere of Earth, the Planets and Their Satellites* (Oxford, Clarendon, 1991).

[4] B. Boudaïffa, P. Cloutier, D. Hunting, M. A. Huels, and L. Sanche, Science **287**, 1658 (2000).

[5] A. Florescu-Mitchell and J. Mitchell, Physics Reports **430**, 277 (2006).

[6] R. L. Platzman, Radiation Research **17**, 419 (1962).

[7] Y. Hatano, Physics Reports **313**, 110 (1999).

[8] H. Nakamura, International Reviews in Physical Chemistry **10**, 123 (1991).

[9] A. Rundquist, C. G. Durfee, Z. Chang, C. Herne, S. Backus, M. M. Murnane, and H. C. Kapteyn, Science **280**, 1412 (1998).

[10] E. Gagnon, P. Ranitovic, X.-M. Tong, C. L. Cocke, M. M. Murnane, H. C. Kapteyn, and A. S. Sandhu, Science **317**, 1374 (2007).

[11] A. S. Sandhu, E. Gagnon, R. Santra, V. Sharma, W. Li, P. Ho, P. Ranitovic, C. L. Cocke, M. M. Murnane, and H. C. Kapteyn, Science **322**, 1081 (2008).

[12] H. Timmers, Z. Li, N. Shivaram, R. Santra, O. Vendrell, and A. Sandhu, Physical Review Letters **113**, 113003 (2014).

[13] F. Calegari, D. Ayuso, A. Trabattoni, L. Belshaw, S. De Camillis, S. Anumula, F. Frassetto, L. Poletto, A. Palacios, P. Decleva, J. B. Greenwood, F. Martin, and M. Nisoli, Science **346**, 336 (2014).

[14] D. M. Villeneuve, P. Hockett, M. J. J. Vrakking, and H. Niikura, Science **356**, 1150 (2017).

[15] L. Cattaneo, J. Vos, R. Y. Bello, A. Palacios, S. Heuser, L. Pedrelli, M. Lucchini, C. Cirelli, F. Martín, and U. Keller, Nature Physics **14**, 733 (2018).

[16] H. Timmers, N. Shivaram, and A. Sandhu, Physical Review Letters **109**, 173001 (2012).

[17] B. Doughty, C. J. Koh, L. H. Haber, and S. R. Leone, Journal of Chemical Physics **136**, 214303 (2012).

[18] C.-T. Liao, X. Li, D. J. Haxton, T. N. Rescigno, R. R. Lucchese, C. W. McCurdy, and A. Sandhu, Physical Review A **95**, 043427 (2017), 1611.05535.

[19] K. Codling and R. P. Madden, The Journal of Chemical Physics **42**, 3935 (1965).

[20] C. Robert Wu, Journal of Quantitative Spectroscopy and Radiative Transfer **37**, 1 (1987).

[21] P. M. Dehmer and W. A. Chupka, The Journal of Chemical Physics **62**, 4525 (1975).

[22] D. Holland, D. Shaw, S. McSweeney, M. MacDonald, A. Hopkirk, and M. Hayes, Chemical Physics **173**, 315 (1993).

[23] M. Richard-Viard, O. Dutuit, M. Lavollée, T. Govers, P. M. Guyon, and J. Durup, The Journal of Chemical Physics **82**, 4054 (1985).

[24] T. Akahori, Y. Morioka, M. Watanabe, T. Hayaishi, K. Ito, and M. Nakamura, Journal of Physics B: Atomic and Molecular Physics **18**, 2219 (1985).

[25] K. Ellis, R. I. Hall, L. Avaldi, G. Dawber, A. McConkey, L. Andric, and G. C. King, Journal of Physics B: Atomic, Molecular and Optical Physics **27**, 3415 (1994).

[26] A. Padmanabhan, M. A. MacDonald, C. H. Ryan, L. Zuin, and T. J. Reddish, Journal of Physics B: Atomic, Molecular and Optical Physics **43**, 165204 (2010).

[27] T. Hayaishi, Y. Iida, Y. Morioka, M. Sasanuma, E. Ishiguro, and M. Nakamura, Journal of Physics B: Atomic and Molecular Physics **19**, 2861 (1986).

[28] Y. Lu, Z. He, J. Cutler, S. Southworth, W. Stolte, and J. Samson, Journal of Electron Spectroscopy and Related Phenomena **94**, 135 (1998).

[29] A. A. Wills, A. A. Cafolla, and J. Comer, Journal of Physics B: Atomic, Molecular and Optical Physics **24**, 3989 (1991).

[30] P. Baltzer, B. Wannberg, L. Karlsson, M. Carlsson Göthe, and M. Larsson, Physical Review A **45**, 4374 (1992).

[31] M. Ukai, N. Kouchi, K. Kameta, N. Terazawa, Y. Chikahiro, Y. Hatano, and K. Tanaka, Chemical Physics Letters **195**, 298 (1992).

[32] P. Erman, A. Karawajczyk, E. Rachlew-Källne, S. L. Sorensen, and C. Strömholm, Physica Scripta **49**, 308 (1994).

[33] M. Ukai, S. Machida, K. Kameta, M. Kitajima, N. Kouchi, Y. Hatano, and K. Ito, Physical Review Letters **74**, 239 (1995).

[34] H. Liebel, S. Lauer, F. Vollweiler, R. Müller-Albrecht, A. Ehresmann, H. Schmoranzer, G. Mentzel, K.-H. Schartner, and O. Wilhelmi, Physics Letters A **267**, 357 (2000).

[35] A. Ehresmann, L. Werner, S. Klumpp, H. Schmoranzer, P. V. Demekhin, B. M. Lagutin, V. L. Sukhorukov, S. Mickat, S. Kammer, B. Zimmermann, and K.-H. Schartner, Journal of Physics B: Atomic, Molecular and Optical Physics **37**, 4405 (2004).

[36] F. Merkt, P. Guyon, and J. Hepburn, Chemical Physics **173**, 479 (1993).

[37] A. Lafosse, J. C. Brenot, A. V. Golovin, P. M. Guyon, K. Hoejrup, J. C. Houver, M. Lebech, and D. Dowek, The Journal of Chemical Physics **114**, 6605 (2001).

[38] Y. Hikosaka, P. Lablanquie, M. Ahmad, R. I. Hall, J. G. Lambourne, F. Penent, and J. H. D.

Eland, Journal of Physics B: Atomic, Molecular and Optical Physics **36**, 4311 (2003).

[39] X. Tang, G. A. Garcia, and L. Nahon, The Journal of Chemical Physics **148**, 124309 (2018).

[40] P. V. Demekhin, D. V. Omel'yanenko, B. M. Lagutin, V. L. Sukhorukov, L. Werner, A. Ehresmann, K.-H. Schartner, and H. Schmoranzer, Optics and Spectroscopy **102**, 318 (2007).

[41] H. Liu, D. Shi, J. Sun, and Z. Zhu, Molecular Physics **113**, 120 (2015).

[42] M. A. Dillon and D. Spence, The Journal of Chemical Physics **74**, 6070 (1981).

[43] L.-L. Fan, Z.-P. Zhong, L.-F. Zhu, X.-J. Liu, Z.-S. Yuan, J.-M. Sun, and K.-Z. Xu, Physical Review A **71**, 032704 (2005).

[44] M. Evans, S. Stimson, C. Y. Ng, and C.-W. Hsu, The Journal of Chemical Physics **109**, 1285 (1998).

[45] H. Liebel, A. Ehresmann, H. Schmoranzer, P. V. Demekhin, B. M. Lagutin, and V. L. Sukhorukov, Journal of Physics B: Atomic, Molecular and Optical Physics **35**, 895 (2002).

[46] G. A. Garcia, L. Nahon, and I. Powis, Review of Scientific Instruments **75**, 4989 (2004).

[47] H.-J. Werner, P. J. Knowles, G. Knizia, F. R. Manby, and M. Schütz, WIREs Comput Mol Sci **2**, 242 (2012).

[48] H.-J. Werner, P. J. Knowles, G. Knizia, F. R. Manby, M. Schütz, *et al.*, "Molpro, version 2015.1, a package of ab initio programs," (2015), see http://www.molpro.net.

[49] Molecular Rydberg states with $^2\Pi_g$ ion core can also be populated by the XUV pulse, potentially dissociating into a 4p excited atomic fragment with a ^2D ion core. However, this atomic state lies above the ionization potential and is expected to autoionize on very short timescales without contributing to the observed signal.

[50] R. E. Stratmann and R. R. Lucchese, Journal of Chemical Physics **102**, 8493 (1995).

[51] R. E. Stratmann, R. W. Zurales, and R. R. Lucchese, Journal of Chemical Physics **104**, 8989 (1996).

[52] U. Fano, Phys. Rev. **124**, 1866 (1961).

[53] J. Berkowitz, *Photoabsorption, Photoionization, and Photoelectron Spectroscopy* (Academic, New York, 1979) p. 10.